Silicon (2024) 16:3343–3357
https://doi.org/10.1007/s12633-024-02920-1

RESEARCH

Device Engineering of Lead-free Double Perovskite ($Cs_4CuSb_2Cl_{12}$ & $Cs_2AgBiBr_6$)/Crystalline Silicon High-Performance Eco-friendly Tandem Solar Cells

Pritam Kumar[1] · Amitesh Kumar[1]

Received: 27 November 2023 / Accepted: 15 February 2024 / Published online: 2 March 2024

Abstract

Lead-free double perovskites are a newly developed category of non-toxic material with impressive photoelectric properties and excellent inherent environmental stability. This study explores the design and performance optimization of lead-free double perovskite/c-Si tandem devices (TDs). Two top cells (TCs) made of $Cs_4CuSb_2Cl_{12}$ (bandgap of 1.6 eV) and $Cs_2AgBiBr_6$ (bandgap of 2.05 eV) absorber materials and the bottom cell (BC) of c-Si (bandgap of 1.12 eV), have been utilized for designing two TDs. To design an efficient TD's structure, TC and BC were first individually simulated and calibrated against the findings derived from the reported experimental data. The absorber's thickness of TC reaches the current matching, when the current it generates under AM 1.5G spectrum matches the BC's current under a filtered spectrum (generated through TC). At current matching condition, the optimized values of thickness of $Cs_4CuSb_2Cl_{12}$ and $Cs_2AgBiBr_6$ layers are 0.418 and 1.29 µm, respectively. The lead-free $Cs_4CuSb_2Cl_{12}/c-Si$ and $Cs_2AgBiBr_6/c-Si$ TDs exhibit a PCE (power conversion efficiency) value of 34.67% (V_{OC} = 1.82 V, J_{SC} = 20.75 mA/cm^2, FF = 88.31%) and 36.88% (V_{OC} = 2.16 V, J_{SC} = 21.105 mA/cm^2, FF = 79.68%), respectively. Performance parameters of TDs obtained from this work are comparable to the results of reported experiments and simulations. Analysis of this study reveals that enhancing PCE of double-perovskite TC is essential to promise the TD's benefits. The results reported demonstrate that lead-free and stable double perovskite materials can act as an essential absorber in sub-cells for highly efficient, commercially viable, non-toxic and eco-friendly tandem photovoltaic technologies.

Keywords Current matching · $Cs_4CuSb_2Cl_{12}$ · $Cs_2AgBiBr_6$ · Lead-free double perovskite · Power conversion efficiency (PCE) · Tandem solar device

1 Introduction

The need to develop more efficient, cost-effective, and eco-friendly renewable energy sources is growing as a result of the rising energy demand, which has led to major environmental concerns. Photovoltaic (PV) technology is widely recognized as one of the cleanest and most sustainable energy options available. It enables the direct transformation of solar energy into electricity. Silicon (Si)-PV, presently dominating the PV industry, has achieved an efficiency milestone of 26.7% [1, 2], approaching the 33% limit (Schokley-Queisser limit) for single-junction PV/ solar cells [3, 4]. To address this limitation, the combination of multiple single-junction PV cells, each having distinct bandgaps, to form a multi-junction or tandem device (TD), enables a broader absorption of photons from the solar spectrum while minimizing energy loss [5, 6]. Under AM 1.5G illumination, it is theoretically possible for an infinite stack of junctions to attain a power conversion efficiency (PCE) of 65.4%. This suggests the potential for highly efficient energy conversion in multi-junction solar cell configurations [7]. Tandem solar cells (TSCs) exist in many design configurations based on their electrical connections and manufacturing processes. The electrical series connection of top cell (TC) and bottom cell (BC) in TSCs ensures that current passing through both cells remains constant [8, 9]. Several tandem solar device configurations are still being thoroughly explored.

✉ Amitesh Kumar
amitesh.ee@nitp.ac.in

1 Nextgen Adaptive Systems Group, Department of Electrical Engineering, National Institute of Technology Patna, Bihar 800005, India

Perovskite solar cells (PSCs) present favourable choices for integration into TDs owing to their outstanding absorption, bandgap tuning capabilities, and affordable deposition methods [10, 11]. Perovskite has successfully been used in demonstrations of high-efficiency Si-based TDs. The investigation of Perovskite/Si TDs to improve PCE has been promising [12]. Perovskite/Si TDs (both monolithic, as well as mechanically stacked) are commercially feasible technologies in recent times, showing PCE of more than 30% [13]. Recent breakthroughs in organic-inorganic halide PSCs have resulted in a significant increase in PCE, escalating from a mere 3% in 2006 to an impressive 25.8% at present [14–17]. Despite their rapid efficiency improvements, PSCs face persistent challenges that hinder their transition into a competitive market viability [18–20]. The primary concerns revolve around the toxicity and stability issues associated with lead-based PSCs, posing obstacles to their widespread commercialization [21]. In addressing these concerns, tin (Sn), which shares a comparable atomic size, has been considered as a substitute for lead (Pb), forming $ASnX_3$ structures in lead-free lead-free PSCs. Sn-based PSCs often exhibit lower efficiencies than lead-based counterparts, due to the inherent instability of Sn^{2+} ions, prone to oxidation and transformation into Sn^{4+}. This oxidation adversely affects material stability, posing a significant challenge in improving performance [21, 22]. Developing novel stable and lead-free perovskites for PV applications remains challenging. Introducing a double perovskite structure offers a potential avenue for expanding perovskite applications in photovoltaics. This entails replacing two Pb^{2+} ions with one M^+ and one M^{3+} ions, resulting in an $A_2M^+M^{3+}X_6$ double perovskite structure [23]. Experiments have demonstrated $Cs_2AgBiBr_6$ and $Cs_4CuSb_2Cl_{12}$ are the most typical stable and lead-free double perovskites [24–26]. The reported theoretical optimized PCE of a $Cs_2AgBiBr_6$and $Cs_4CuSb_2Cl_{12}$based solar cells are up to 11.69% [24] and 30% [26], respectively. A lead-free and stable tandem solar device with enhanced performance has to be developed.

Two lead-free double perovskite/c-Si (crystalline Si) TSCs utilizing $Cs_4CuSb_2Cl_{12}$ and $Cs_2AgBiBr_6$ as the TC's absorber layers have been designed and investigated in this work. In tandem configuration, TC comprises a Hole Transport Layer (HTL), a double perovskite film serving as the absorber, and an Electron Transport Layer (ETL). Both TC (ETL/Absorber/HTL) and BC (c-Si: n+ / p / p+) have been connected in series configuration to construct a two-terminal (2-T) TD. Numerical designs of the devices were conducted using SCAPS-1D (Solar Cell Capacitance Simulator), initially simulating standalone models for both TC and BC, subsequently calibrating them with reported experimental data from existing literature. Furthermore, investigations were undertaken to optimize results by tuning parameters related to the TC's absorber layer and interfaces. The thickness of the TC's absorber layer is tuned to ensure current matching between the cells. By ensuring current matching conditions, the performance of TD models can be analyzed through device designs of both TC and BC models under the AM 1.5G solar spectrum, and the filtered spectrum, respectively. These designs provide valuable insights into the overall performance of the device, playing a key role in advancing TSC technology. The efficacy of the designed TD models has been validated by comparing their performance with experimental, as well as simulated results reported in existing literature.

In Section 2, the device structure is outlined, elucidating essential input/model parameters for each individual layer. Section 3 delves into the calibration of the sub-cells and outlines the numerical methodology for designing the TDs. Further, the obtained results for lead-free double perovskite/c-Si TDs are presented and discussed in Section 4, followed by a comparison with the recently reported results in Section 5.

2 Device Structure and Model Parameters

The schematic diagram for lead-free double perovskite/c-Si (crystalline silicon) TD is represented in Fig. 1. In the proposed TD, the BC is in fact a c-Si solar cell, while the TC is a lead-free double perovskite-based solar cell. Both sub-cells are joined together in a series configuration to form a 2-T TD. Illumination with the AM 1.5G solar spectrum is directed towards TC, whereas BC is subjected to a filtered

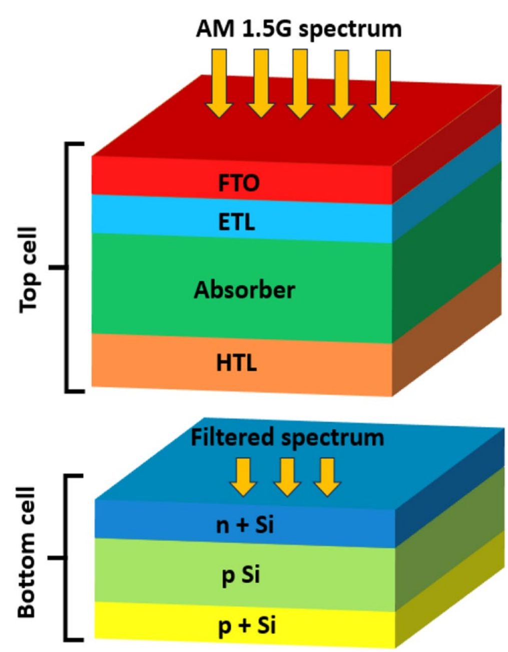

Fig. 1 Schematic representation for lead-free double perovskite/c-Si TD

Table 1 Device structures for proposed TC, BC and TD models

Cell	Device structure	ID
BC	n + Si/pSi/p + Si	c-Si
TC (ETL/Absorber/HTL)	$TiO_2/Cs_4CuSb_2Cl_{12}/Cu_2O$	TC-1
	$Zn_{0.75}Mg_{0.25}O/Cs_2AgBiBr_6/Cu : Ni_{1-x}O$	TC-2
TD (TC/BC)	TC-1/c-Si	TD-1
	TC-2/c-Si	TD-2

spectrum generated from the TC. The structure of TC includes a front contact incorporating FTO (Fluorine-doped tin oxide), ETL, lead-free double perovskite film (absorber layer), HTL, and a metallic back contact (Au). For designing of TD, the selected materials for different layers of TC are: TiO_2 and $Zn_{0.75}Mg_{0.25}O$ as ETL, lead-free double perovskites $Cs_4CuSb_2Cl_{12}$ and $Cs_2AgBiBr_6$ as absorber layer, and Cu_2O and Cu: $Ni_{1-x}O$ as HTL. Having good photoelectric properties and innate stability, double perovskites are a novel kind of material [24–26]. BC has a base layer that is moderately doped p-type, an emitter that is highly doped p-type, and an n+ (highly doped n-type) layer that serves as BSF (back surface field).

The device structures of the proposed TC, BC and TD models are represented in Table 1. The bandgaps of absorber layers of TC-1 ($Cs_4CuSb_2Cl_{12}$ as absorber) and TC-2 ($Cs_2AgBiBr_6$ as absorber) are 1.6 and 2.05 eV, respectively. All layers of BC have a band gap of 1.12 eV. This study uses SCAPS software, and Tables 2, 3 and 4 list the basic input/model parameters of different layers in sub-cells and interfaces after being carefully choosen from published literature and experimental works [24, 26–31]. All layers, along with interfaces like absorber/HTL and ETL/absorber, are subjected to neutral defects characterized by a single energetic distribution. Figure 2a and b depict energy band diagrams (EBDs) of the diverse materials utilized in sub-cell's design, offering insights into their respective

Table 2 Input parameters for different layers of TCs

TC	TC-1				TC-2			
Parameters	FTO	TiO_2	$Cs_4CuSb_2Cl_{12}$	Cu_2O	FTO	$Zn_{0.75}Mg_{0.25}O$	$Cs_2AgBiBr_6$	$Cu : Ni_{1-x}O$
Thickness (nm)	500	30	200 (varied)	200	30	30	200 (varied)	98
Bandgap (eV)	3.2	3.2	1.6	2.17	3.5	3.82	2.05	3.89
Electron affinity (eV)	4.4	4	3.74	3	4	4.03	4.19	1.56
Permittivity	9	9	10	7.5	9	9	5.8	11.7
Effective CB density (cm^{-3})	2.2×10^{18}	1×10^{21}	4.5×10^{19}	2.0×10^{18}	2.2×10^{18}	1×10^{15}	1×10^{16}	3.78×10^{16}
Effective VB density (cm^{-3})	1.8×10^{19}	2×10^{20}	1.6×10^{19}	1.1×10^{19}	1.8×10^{19}	1×10^{16}	1×10^{16}	3.78×10^{16}
Electron velocity (cm/s)	1.0×10^7	1.0×10^7	1.0×10^7	1.0×10^7	1.0×10^7	1.0×10^7	1.0×10^7	1.0×10^7
Hole velocity (cm/s)	1.0×10^7	1.0×10^7	1.0×10^7	1.0×10^7	1.0×10^7	1.0×10^7	1.0×10^7	1.0×10^7
Electron mobility (cm^2/Vs)	20	0.006	2.5	200	20	50	11.81	5.58
Hole mobility (cm^2/Vs)	10	0.006	2.5	80	10	20	0.49	5.58
Donor density (cm^{-3})	1.0×10^{19}	5.06×10^{19}	-	-	1.0×10^{18}	1.0×10^{16}	1.0×10^{19}	-
Acceptor density (cm^{-3})	-	-	1.0×10^{13}	2.0×10^{19}	-	-	1.0×10^{19}	3.0×10^{18}
Defect density (cm^{-3})	1.0×10^{14}	1.0×10^{15}	1.0×10^{13}	1.0×10^{15}	1.0×10^{15}	1.0×10^{15}	1.0×10^{15}	1.0×10^{14}
Extinction coefficient (k)	0.117	0.116	0.304	0.226	0.083	0.027	0.239	0.005
Refractive index (n)	3.002	3.002	3.176	2.747	3.001	3.0	2.42	3.42

Table 3 Input settings for TC's absorber/HTL and ETL/absorber interfaces

TC	TC-1		TC-2	
Parameters	$Cs_4CuSb_2Cl_{12}/Cu_2O$	$TiO_2/Cs_4CuSb_2Cl_{12}$	$Cs_2AgBiBr_6/Cu : Ni_{1-x}O$	$Zn_{0.75}Mg_{0.25}O/Cs_2AgBiBr_6$
Defect type	Neutral	Neutral	Neutral	Neutral
Capture cross section for electrons (cm^2)	3.22×10^{-18}	3.22×10^{-18}	3.22×10^{-18}	3.22×10^{-18}
Capture cross section for holes (cm^2)	3.22×10^{-18}	3.22×10^{-18}	3.22×10^{-18}	3.22×10^{-18}
Energetic distribution	Single	Single	Single	Single
Energy with respect to reference (eV)	1.3	1.3	1.3	1.3
Total density (cm^{-2})	2.3×10^{10}	2.3×10^{10}	2.3×10^{10}	2.3×10^{10}

Table 4 Input parameters of different layers of BC

Parameters	n + Si	p Si	p + Si
Thickness (μm)	0.2	0.3	0.1
Bandgap (eV)	1.12	1.12	1.12
Electron affinity (eV)	4.05	4.05	4.05
Permittivity	11.9	11.9	11.9
Effective CB density (cm^{-3})	2.8×10^{19}	2.8×10^{19}	2.8×10^{19}
Effective VB density (cm^{-3})	1.04×10^{19}	1.04×10^{19}	1.04×10^{19}
Electron velocity (cm/s)	1.0×10^{7}	1.0×10^{7}	1.0×10^{7}
Hole velocity (cm/s)	1.0×10^{7}	1.0×10^{7}	1.0×10^{7}
Electron mobility (cm^2/Vs)	1400	1400	1400
Hole mobility (cm^2/Vs)	450	450	450
Donor density (cm^{-3})	1.0×10^{20}	-	-
Acceptor density (cm^{-3})	-	1.0×10^{16}	1.0×10^{20}
Defect density (cm^{-3})	-	-	-

energy band structures. The minimum energy levels of VB (valence band) and CB (conduction band) in the EBD are represented by the lower and upper boundaries for each utilized materials, respectively. The refractive index (n) and extinction coefficient (k) of various layers in the top cells have been calculated using the methods outlined in the literature [32, 33] and are listed in Table 2 at a wavelength of 320 nm.

3 Device Design

In this work, numerical designs of lead-free double perovskite/c-Si TDs are implemented through the utilization of SCAPS-1D software, specifically version 3.3.10. This software relies on three fundamental semiconductor equations: Poisson's equation, hole and electron continuity equations, collectively elucidating the mechanisms of carrier generation and recombination within device layers [34]. The optical and recombination models integrated into SCAPS are showcased in Table 5. The similarities between the simulated results from this software and the experimental findings reported in numerous literature works are evident. SCAPS-1D simulator does not entirely allow simulating a photovoltaic device featuring a multijunction configuration. In multijunction modelling, it is a frequent assumption that the tunnel junction is ideal. It is assumed that there are negligible optical and electrical losses at interfaces of considered TDs under the present study. The device models of standalone TCs and BC have initially been calibrated making use of existing experimental settings from literature, as detailed in Tables 2, 3 and 4. The performance parameters of calibrated models along with the results derived from the reported experimental observations, are mentioned and compared in Table 6. Figure 3 illustrates the J-V characteristics of the designed standalone device structures in comparison with published measurement. The obtained performance parameters follow the reported measurements [24, 25, 37]. By calibrating the standalone both the sub-cells, this study ensures high accuracy in reflecting the real values. Further optimization of absorber thickness is required to boost TC performance. For TC to perform better, absorber thickness needs to be further optimized. It is necessary to point out that parameter values are optimized for different layers except thickness of absorber layer and listed in Tables 2, 3 and 4. A tandem solar device's sub-cells can be considered a pair of series-connected diodes. While analyzing the performance of TDs, TC and BC are simulated separately to obtained current matching points. The J-V characteristics of TD are then determined by treating them as an equivalent series connection. The device design of TC (wide bandgap) is performed using AM1.5G solar spectrum, while BC (narrow bandgap) is designed utilizing a filtered spectrum derived from TC. The filtered/transmitted spectrum, $S(\lambda)$ (from TC to BC) is calculated using Eq. (1) [30, 38]:

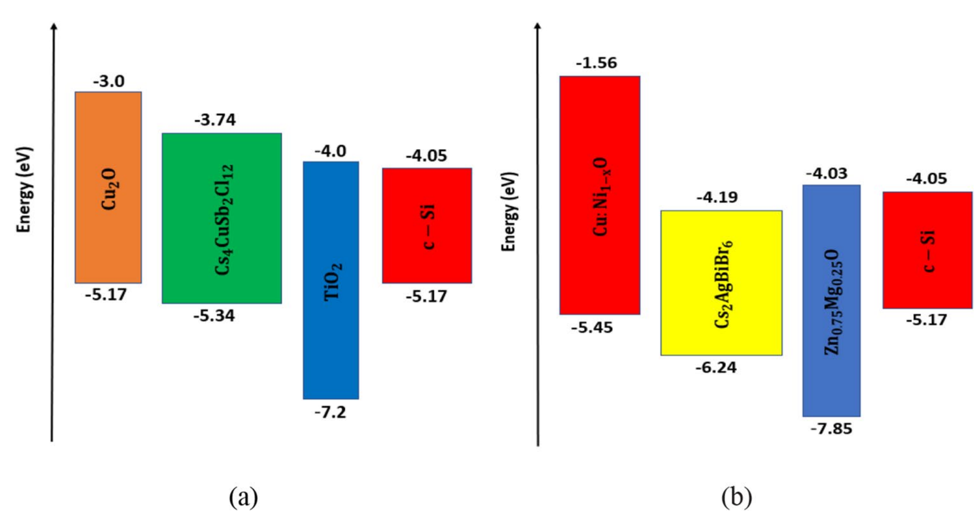

Fig. 2 Illustration of EBDs for materials utilized in **a** TD-1, and **b** TD-2 configurations

Table 5 Optical and recombination models utilized in SCAPS simulation

Optical model	Recombination model
The optical model utilized to compute generation of electron-hole (eh) pairs from incident photon flux comprises following equations [35]: $N_{phot}(\lambda,x) = N_{phot0}(\lambda).T_{front}(\lambda).\exp(-x\alpha(\lambda)).\frac{1+R_{back}(\lambda).\exp(-2(d-x)\alpha(\lambda))}{1-R_{back}(\lambda).R_{int}.\exp(-2d\alpha(\lambda))}$ $G(\lambda,x) = \alpha(\lambda,x).N_{phot}(\lambda,x)$ $G(x) = \int_{\lambda_{min}}^{\lambda_{max}} G(\lambda,x)d\lambda = \int_{\lambda_{min}}^{\lambda_{max}} \alpha(\lambda,x).N_{phot}(\lambda,x)d\lambda$ Where, $N_{phot}(\lambda,x)$ signifies the photon flux at each position in the layer, $N_{phot0}(\lambda)$ denotes the incident photon flux, and at each wavelength, $T_{front}(\lambda)$ represents the transmission of the front contact, $\alpha(\lambda)$ stands for the absorption coefficient, R_{int} stands for the internal reflection at the front contact, R_{back}signifies the reflection at the back contact, λ represents wavelength, d represents the layer thickness, x represents the position in the layer, and $G(x)$ denotes the generation rate of electron-hole pairs.	In SCAPS simulation, the introduction of three distinct recombination processes: Shockley-Read-Hall (SRH) recombination, radiative recombination, and Auger recombination is facilitated through the utilization of the following equations [34, 36]: $R_{SRH} = \frac{np-n_i^2}{\tau_p(n+n_0)+\tau_n(p+p_0)}$ $R_{radiative} = K(np - n_i^2)$ $R_{Auger} = (C_n n + C_p p)(np - n_i^2)$ Where, R_{SRH}, $R_{radiative}$ and R_{Auger} denote the SRH, radiative, and Auger recombination rates, respectively, with n and p representing the concentrations of electrons and holes in the conduction and valence bands, n_0 and p_0 denoting the equilibrium concentrations, τ_n andτ_p signifying the lifetimes of electrons and holes, n_i representing intrinsic carrier concentration, and K, C_n and C_P are the radiative recombination coefficient, Auger electron and hole capture coefficients, respectively.

Table 6 Calibration of standalone TCs and BC using experimental parameters

Device structure	V_{OC} (V)	$J_{SC}(mA/cm^2)$	FF (%)	PCE (%)	Reference/ID
n + Si/pSi/p + Si	0.74	42.30	83.8	26.35	[32]
n + Si/pSi/p + Si	0.75	40.52	85.25	26.09	c-Si
$TiO_2/Cs_4CuSb_2Cl_{12}$ nanocrystals/Cu_2O	1.03	19.07	82.01	16.11	[25]
$TiO_2/Cs_4CuSb_2Cl_{12}/Cu_2O$	1.09	15.91	88.66	15.38	TC-1
$SnO_2/Cs_2AgBiBr_6/Cu_2O$	1.97	6.39	89.5	11.32	[24]
$Zn_{0.75}Mg_{0.25}O/Cs_2AgBiBr_6/Cu : Ni_{1-x}O$	1.42	9.65	87.21	11.99	TC-2

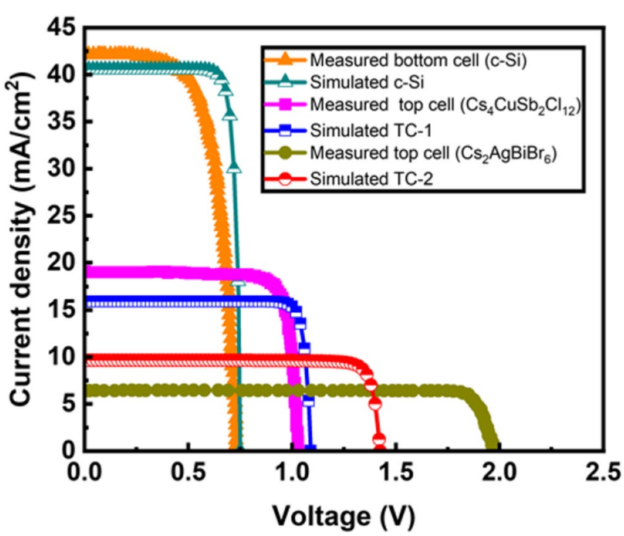

Fig. 3 J-V curves of standalone TCs and BC along with published measurements

$$S(\lambda) = S_0(\lambda).\exp\left(\sum_{i=1}^{4} -\alpha_{layer_i}(\lambda).d_{layer_i}\right) \quad (1)$$

where $S_0(\lambda)$ denotes AM 1.5G solar spectrum, $\alpha(\lambda)$ represents absorption coefficient, λ signifies wavelength, d stands for thickness of the several layers in TC, and $layer_i$refers to a specific layer ($i = 1$ corresponds to FTO, 2 to ETL, 3 to absorber, and 4 to HTL). $\alpha(\lambda)$ for different layers of the TC are depicted in Fig. 4, which are used in Eq. (1). The current matching requirement is essential because inadequate current matching between TC and BC may result in an accumulation of surplus charge carriers at the recombination interface, negatively impacting recombination behavior [39]. Achieving current matching between the TC and BC in a tandem configuration involves fine-tuning of TC's thickness to ensure that its current, generated under the AM1.5G solar spectrum, matches BC's current under a filtered spectrum corresponding to TC. The minimal current obtained from TC and BC defines the tandem current's value i.e., current matching point. This matching point can greatly boost the tandem cell's performance. The two cells can generate more

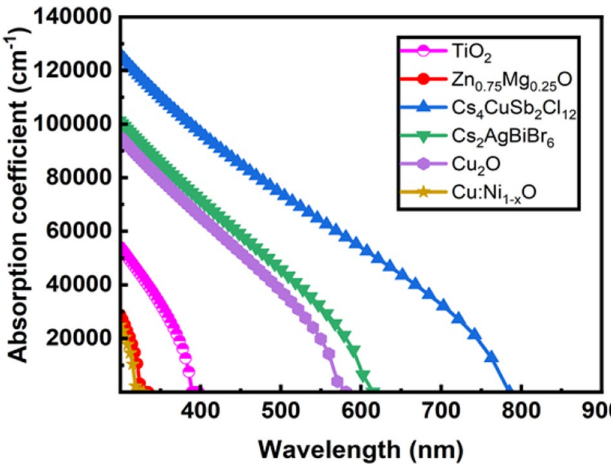

Fig. 4 Absorption coefficients of different layers of the TCs

current when this point is raised, contributing to an improvement in the overall PCE of TD.

4 Results and Discussion

A 2-T, TD is a series connection of a TC and a BC, as described in Section 3. Thus, TD's V_{OC} (open circuit voltage) is the total of its sub-cell voltages. However, the lowest value of junction currents will set a limit on the overall device's J_{SC} (short circuit current density). Device design results of standalone individual cells along with the overall TD are presented and explained in the following Section 4.1 to Section 4.3. For enhancing the overall performance of TD, extensive investigations have also been carried out to explore the performance of double perovskite based TCs. These investigations involve systematic variations of key parameters such as absorber thickness, doping density, defect density, and interface (ETL/absorber and absorber/HTL) defects in Section 4.2 (4.2.1–4.2.4). A comparison of the obtained results with the recently reported results for the designed TDs is showcased in Section 4.5.

4.1 Standalone c-Si BC

In this study, both TD-1 and TD-2 feature a c-Si solar cell as their BC. The thickness values utilized for the n + Si, p Si, and p + Si layers are 0.2 µm, 300 µm, and 10 µm, respectively. The device design of standalone c-Si cell is performed utilizing the AM1.5G solar spectrum, and the device model exhibits PCE = 26.09%. (V_{OC} = 0.75 V, J_{SC} = 42.52 mA/cm^2 and FF = 85.25%,). Table 5 presents the simulated and reported experimental values [37]. Figure 5a displays the BC's simulated J-V plot. The resulting performance parameters closely match the reported experimental values, providing the critical validation of the proposed methodology.

4.2 Standalone Lead-Free Double Perovskite TCs

In this work, two TCs made of $Cs_4CuSb_2Cl_{12}$ (TC-1) and $Cs_2AgBiBr_6$ (TC-2) absorber layers have been utilized for TDs TD-1 and TD-2 respectively. Both TCs (with absorber layer thickness value of 0.2 µm) have been initially simulated under AM1.5G solar spectrum in standalone conditions. The performance parameters of the initial simulation along with the reported experimental results [24, 25] are mentioned and compared in Table 5. The obtained performance parameters agree well with the experimental values that have been published, which is a critical component for validation of proposed method. The results inspire confidence in moving forward with TD simulation. The thickness of the TC's absorber plays a pivotal role in augmenting performance in tandem design. At following thicknesses of various layers, TC's performance is further improved. The layer thicknesses for TC-1: 0.03 µm, 0.7 µm and 0.2 µm of TiO_2 (ETL), $Cs_4CuSb_2Cl_{12}$ (absorber layer) and Cu_2O (HTL) respectively. The layer thicknesses for TC-2: 0.03 µm, 0.5 µm and 0.098 µm of $Zn_{0.75}Mg_{0.25}O$ (ETL), $Cs_2AgBiBr_6$ (absorber layer) and Cu : $Ni_{1-x}O$ with Cu : Ni : O

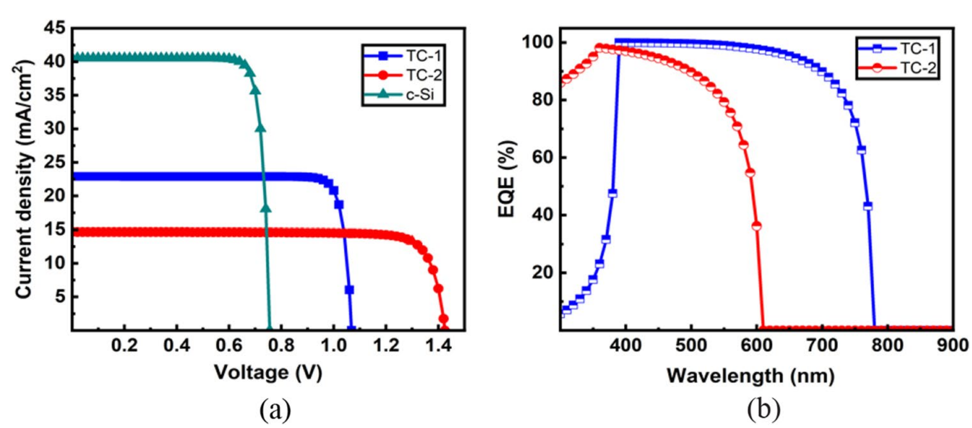

Fig. 5 **a** J-V plots of standalone TCs and BC, and **b** EQE plots of the standalone TCs

ratio of 0.14:0.68:1 (HTL) respectively. The TC-1 and TC-2 cell models exhibit PCE of 21.49% (V_{OC} = 1.07 V, J_{SC} = 22.90 mA/cm^2, and FF = 87.80%), and 17.48% (V_{OC} = 1.42 V, J_{SC} = 14.65 mA/cm^2, and FF = 83.69%) respectively. Figure 5a depicts the simulated J-V curves, while b depicts external quantum efficiency (EQE) curves for both standalone TCs. At a wavelength of 380 nm, TC-2 achieves more than 90% EQE, which then drops to below 65% at wavelengths over 580 nm. When compared to TC-1, TC-2 achieves more than 90% EQE at a lower wavelength. This is a result of the absorber layer of TC-2 having a high bandgap (2.05 eV). As evident from Fig. 5b, the EQE cut-off wavelength is 30% longer in TC-1, resulting in a higher J_{SC}. The simulated EQE value for the TC-2 follows the experimentally measured EQE [30, 40]. Furthermore, the performance of TCs has been investigated by tunning absorber layer as well as interface parameters.

4.2.1 Impact of Tuning Absorber's Thickness

The performance analysis of TCs involves investigating the influence of varying the absorber layer's thickness, ranging from 0.2 to 2 µm. Figure 6a–d illustrate the changes in performance parameters (V_{OC}, J_{SC}, FF, and PCE) with respect to the absorber's thickness. A thin absorber results in poor recombination and a high V_{OC}. It is noticeable that J_{SC} value rises in both cells with the augmentation of the absorber's thickness. This enhancement can be attributed to the amplified absorption of incident photons and a greater number of electron-hole pairs generated. However, beyond a certain thickness, the PCE exhibits a decline. This decrease is associated with the heightened occurrence of recombination processes (radiative, Shockley-Read-Hall, and Auger recombinations) within the absorber material as a result of the thicker layers. Increasing absorber thickness improves carrier generation rate, enhancing efficiency with elevated J_{SC} but also increases recombination rates as carriers cover longer distances, impacting device's performance [41, 42]. These findings highlight the importance of optimizing the absorber layer's thickness to strike a balance between photon absorption (generation rate) and recombination rate, ultimately maximizing the PCE of TCs. The generation and recombination profiles are acquired and presented in Fig. 7a–d, confirming the increased penetration of these rates within the absorber at greater thicknesses. With the optimized thicknesses set at 1.2 and 1.5 µm, TC-1 and TC-2 have attained PCE values of 21.99% and 22.56%, respectively.

4.2.2 Impact of Tuning Absorber's Doping Density

The doping density in absorber layer has been tuned from 10^{12} to 10^{20}cm^{-3} for both cells to see how it affects the performance of the device. Figure 6e–h depict the change in performance parameters with varying doping density of absorber. From Fig. 6e–h, it is evident that the changes in performance parametrs are minimal when the doping density changes for TC-2, while PCE declines with increasing doping density after its value of 10^{13}cm^{-3} for TC-1. The device's overall performance remains relatively stable at lower doping densities, but deteriorates at higher doping densities.The selected values for doping density that yield optimal performance in TC-1 and TC-2 are 10^{13} and 10^{16}cm^{-3}, which exhibit PCE of 21.49% and 17.48%, respectively. To gain a better insight into the impact of doping concentration on performance parameters, the generation and recombination rates are depicted with position in Fig. 7e–h. It is noteworthy that the generation rate shows consistency across various doping levels. Higher doping concentration raises the electric field at absorber interface, improving the separation process but adversely impacting performance due to increased recombination [36, 43].

This demonstrates how improving device performance requires correct doping in the absorber material.

4.2.3 Impact of Tuning Absorber's Defect Density

Increasing defect density results in more point defects in absorber layer, resulting in higher recombination. The lifetime of carriers decreases with more recombination. A rise in recombination diminishes the performance parameters of the device. Experimental methods for calculating these properties include intensity-modulated photovoltage, along with terahertz spectroscopy [44]. To investigate the impact of defect density in absorber layer on device performance, it is changed from 10^{12} to 10^{20}cm^{-3}. PCE for TC-1 and TC-2 decreases by 29.6% and 36.78%, respectively, when defect density increases from 10^{15} to 10^{19}cm^{-3}. This is due to the elevated possibility of recombination as the defect density increases. Figure 6i–l show how performance parameters changed with varying absorber defect densities. The optimum values of defect density are taken for TC-1 and TC-2 are 10^{13} and 10^{15}cm^{-3}, which exhibit PCE of 21.49% and 17.48%, respectively. The analysis of Fig. 6i–l indicates a clear inference that an increase in the defects within the absorber results in a decline in performance parameters. Additionally, Fig. 7i–l portrays the profiles of generation and recombination rates across

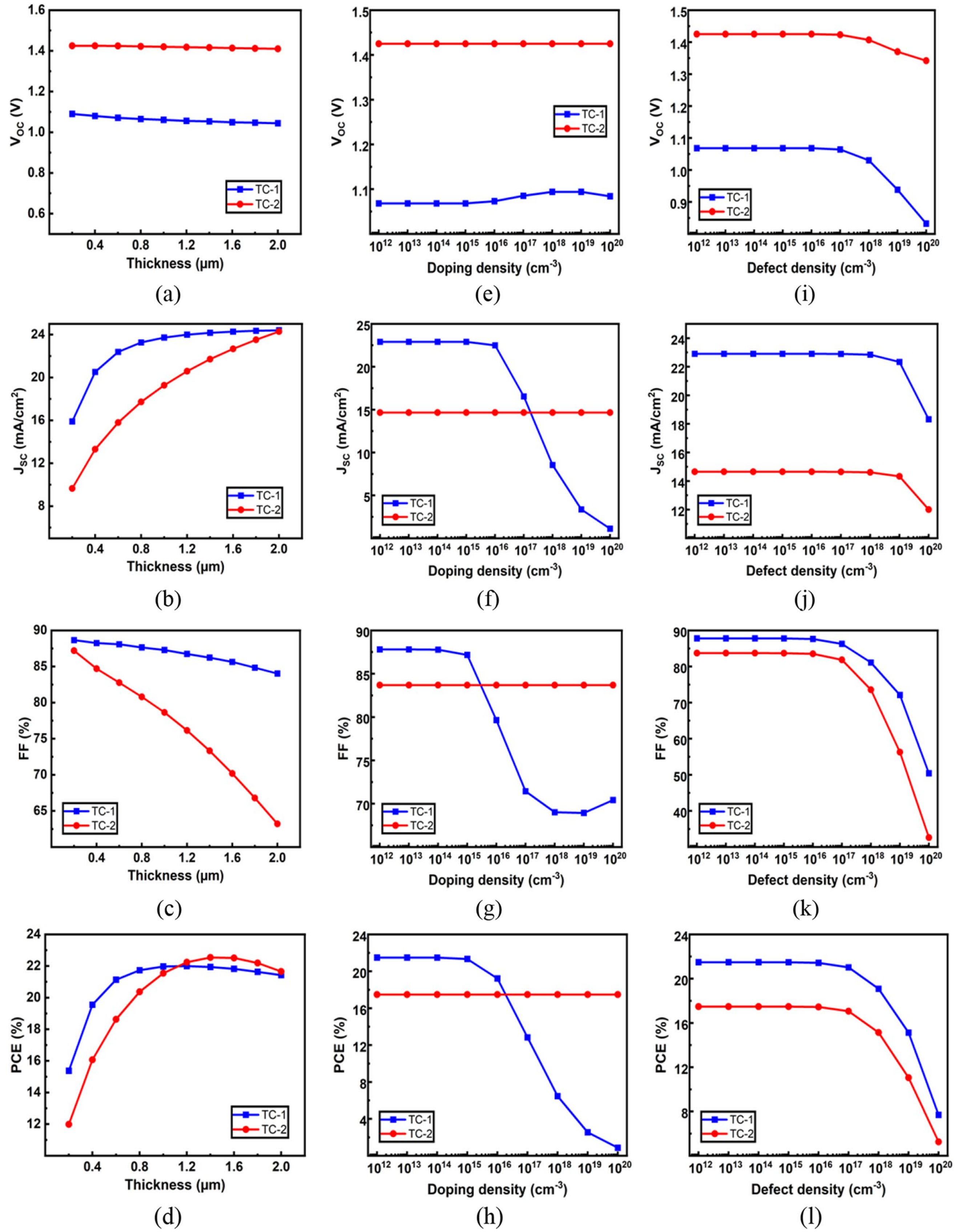

Fig. 6 TC's performance parameters in relation to tuning absorber thickness (**a**–**d**), doping density (**e**–**h**), and defect density (**i**–**l**)

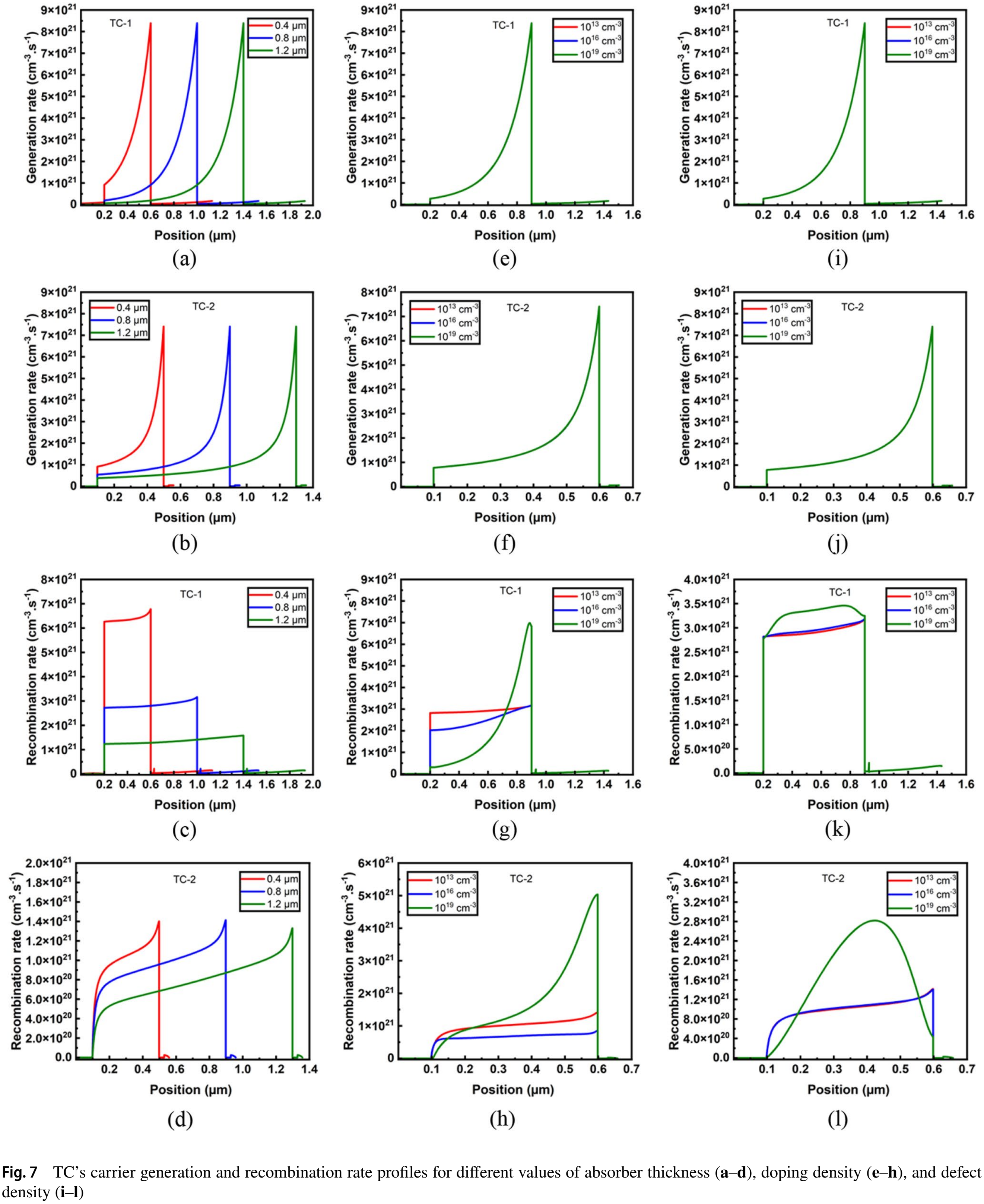

Fig. 7 TC's carrier generation and recombination rate profiles for different values of absorber thickness (**a**–**d**), doping density (**e**–**h**), and defect density (**i**–**l**)

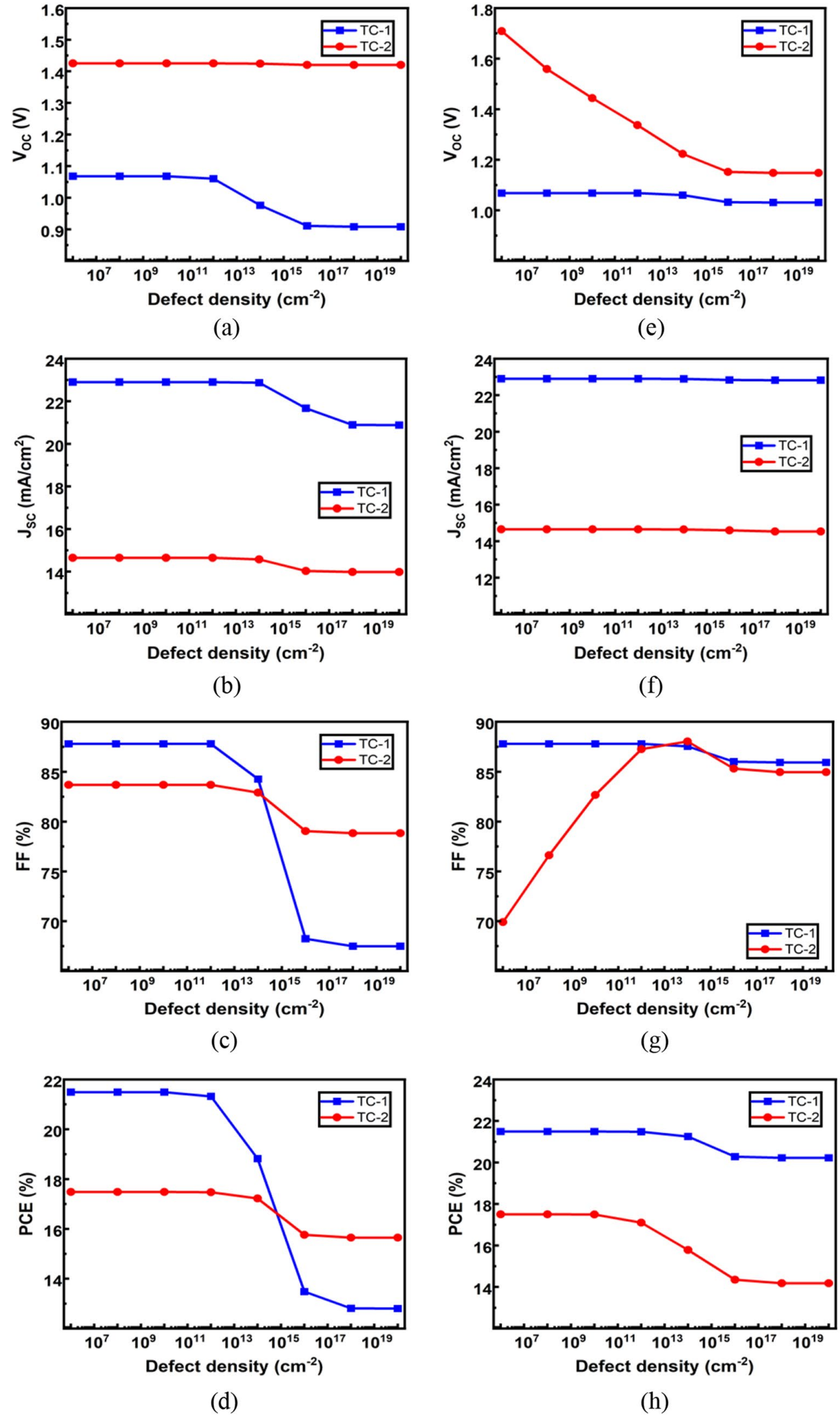

Fig. 8 TC's performance parameters in relation to tuning defect density at ETL/absorber (**a**–**d**), and absorber/HTL (**e**–**h**) interfaces

different defect density values. Notably, the generation rate exhibits stability across varying doping levels. Figure 7k–l highlights the notable influence of defect density on the absorber layer's recombination rate, resulting in increased carrier recombination with higher defect density. As a consequence, there is a reduction in carrier lifetime and diffusion length, contributing to the overall decline in device performance [41, 45].

4.2.4 Impact of Tuning Interface's Defect Density

Reducing carrier recombination within the interface is significant to enhance carrier extraction. The ETL/absorber and absorber/HTL interface defects are varied between 10^6 to $10^{20}cm^{-2}$ to investigate their impact on device performance. The impact of interface defects on TC's performance is clearly illustrated in Fig. 8a–h. Device performance for both cells remain unchanged by ETL/absorber interface defect density below $10^{10}cm^{-2}$, while PCE values for TC-1 and TC-2 decrease by 40.39% and 10.46%, respectively, with a rise in defect levels from 10^{10} to $10^{18}cm^{-2}$. Device performance for both cells remain unchanged by absorber/HTL interface defect level below $10^{12}cm^{-2}$, while PCE values for TC-1 and TC-2 decrease by 5.86% and 17.07%, respectively, with a rise in defect density from 10^{12} to $10^{18}cm^{-2}$.

4.3 Lead-Free Double Perovskite/c-Si TSCs

In order to simulate double perovskite/c-Si TSCs (TDs), a fairly straightforward approach is being adopted. The method for simulating the TD has been explained in Section 3. Due to the fact that sub-cells of a TD can be conceptualized as a pair of diodes electrically coupled in series, ensuring current matching between them is essential. At current matching point, TC and BC possess identical J_{SC} or J_{MP} (current density corresponding to maximum power point) values. The cell having lower J_{SC} value determines the total J_{SC}, and addition of sub-cell's V_{OC} values provides total V_{OC} for the TDs. Two TDs, TD-1 (TC-1/c-Si) and TD-2 (TC-2/c-Si), have been designed and simulated in this study. The device design of TCs (TC-1 and TC-2) is performed using AM1.5G spectrum, while BC simulation is performed using a filtered spectrum generating through TC. To achieve current matching among sub- cells, TC's absorber thickness is finely adjusted. This tuning process ensures that the TC's current (when exposed to the AM1.5G spectrum), matches the BC's current (generated in the presence of a filtered spectrum). At first, thickness of absorber layer of TC-1 and TC-2 was changed from 0.2 to 2 µm, while thicknesses of the other layers remained fixed. For each value of absorber thickness, a specific filtered spectrum was obtained. Subsequently, this filtered spectrum was employed to illuminate the BC. In Fig. 9, the variations in J_{SC} and J_{MP} values for both the TC and BC are shown as a function of TC's absorber thicknesses. Analysis of Fig. 9 reveals a notable similarity in the trends exhibited by J_{SC} and J_{MP}, indicating a consistent behavior in the underlying device physics. For TD-1, J_{SC} and J_{MP} current matching conditions have been obtained at TC-1's absorber thickness values, 0.418 and 0.41 µm, respectively. For TD-2, J_{SC} and J_{MP} current matching conditions have been obtained at TC-2's absorber thickness values, 1.29 and 1.41 µm, respectively. In Fig. 10, the AM 1.5G spectrum is depicted as the illumination source for TCs, and the filtered spectra (under the conditions of J_{SC} current matching) are shown, utilized in illuminating the BC. With the above J_{SC} matching conditions, lead-free double perovskite/c-Si TDs (TD-1 and TD-2) have been simulated. The resulting J-V plots are presented in Fig. 11, and Table 6 details the performance parameters for the TDs. The TD-1 and TD-2 exhibit PCE of 34.67% (with $V_{OC}=1.82$ V, $J_{SC}=20.75$ mA/cm^2, FF = 88.31%), and 36.88% (with $V_{OC}=2.16$ V, $J_{SC}=21.105$ mA/cm^2, FF = 79.68%), respectively. J_{SC} values for TD-1 and TD-2 are interestingly comparable. The V_{OC} and PCE values of TD-2 are higher as compared to TD-2, likely due to the larger thickness and bandgap values of $Cs_2AgBiBr_6$ compared with $Cs_4CuSb_2Cl_{12}$. Table 7; Fig. 10 make evident that BC (lower J_{SC}) limits the TD's total J_{SC}, and the addition of V_{OC} values of each sub-cell provide the total V_{OC} for both TD-1 and TD-2.

4.4 Comparison with the Recently Reported Results

The comparison of this work with recently reported experimental and simulated results of TDs is shown in Table 8. Performance metrics, including V_{OC}, J_{SC}, FF, and PCE of TDs obtained from this work are comparable to those of the reported experimental and simulated devices [2, 30, 38, 46–49]. The results of this work show that lead-free double perovskite/c-Si TDs can theoretically achieve PCE exceeding 36.88% (TD-2). With regard to performance, this TD structure is an intriguing substitute for conventional silicon solar cells, that offers higher efficiency, better stability, and less expensive manufacturing.

5 Conclusions

This study involves the design and exploration of lead-free TDs incorporating double perovskite/ c-Si structures using SCAPS 1-D. Two lead-free double perovskite materials, $Cs_4CuSb_2Cl_{12}$ and $Cs_2AgBiBr_6$ have been investigated as the absorber materials for TCs, while the BC comprises a c-Si photovoltaic cell. In order to devise an efficient TD structure, a stepwise approach was followed: initially, standalone device designs were done for both TC and BC, after which

Table 7 Performance parameters of TDs, including their respective TC and BC

Cell	V_{OC} (V)	J_{SC} (mA/cm^2)	FF (%)	PCE (%)
TC-1	1.08	20.755	88.23	19.77
c-Si (filtered)	0.74	20.750	85.23	25.61
TD-1 (TC-1/c-Si)	1.82	20.750	88.31	34.67
TC-2	1.42	21.109	74.92	22.42
c-Si (filtered)	0.74	21.105	85.23	25.30
TD-2 (TC-2/c-Si)	2.16	21.105	79.68	36.88

they were coupled in series. To achieve optimal performance, particular attention was given to achieving a current matching condition between sub-cells. This was accomplished by finely tuning the absorber layer thickness of TC until the current generated under AM 1.5G spectrum matched the BC's current obtained under the filtered spectrum specific to the TC's absorption characteristics. After reaching the condition of current matching, the optimized thickness for $Cs_4CuSb_2Cl_{12}$ and $Cs_2AgBiBr_6$ layers are 0.418 and 1.29 µm, respectively. The lead-free $Cs_4CuSb_2Cl_{12}/c-Si$

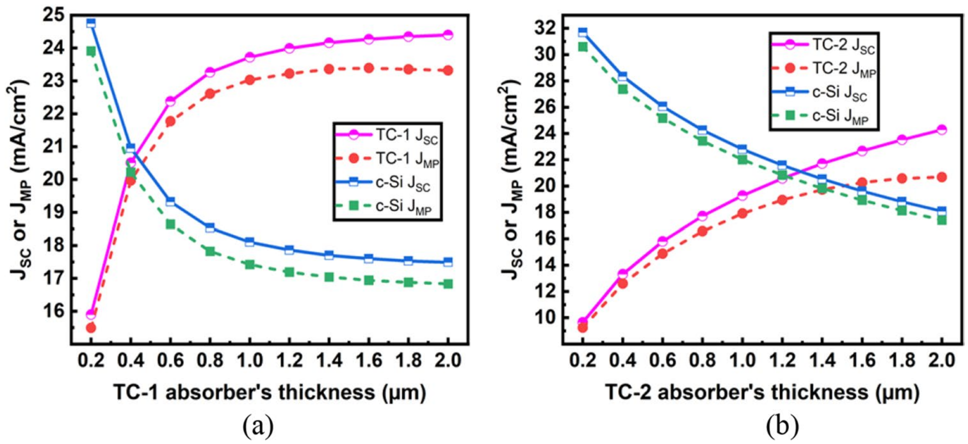

Fig. 9 J_{SC} and J_{MP} values of the TC and BC plotted against TC's absorber thicknesses for **a** TD-1, and **b** TD-2

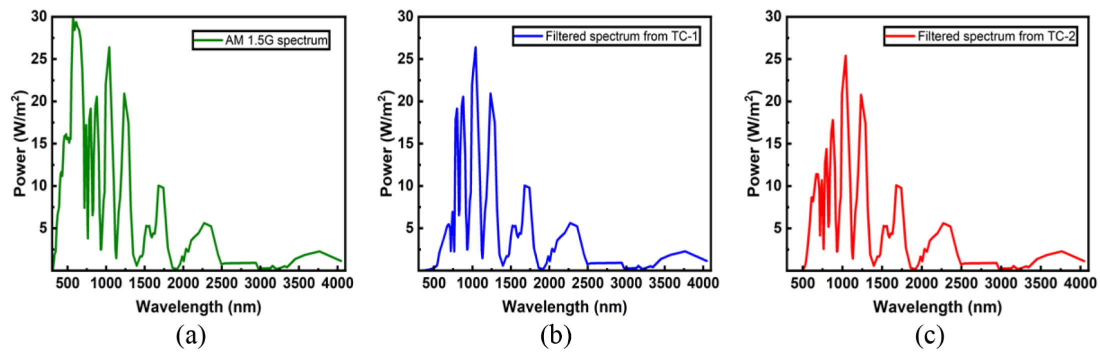

Fig. 10 **a** AM 1.5G spectrum illuminated on the TCs, **b** and **c** filtered spectrum (under J_{SC} current matching conditions) illuminated on the BC transmitted from TC-1 and TC-2

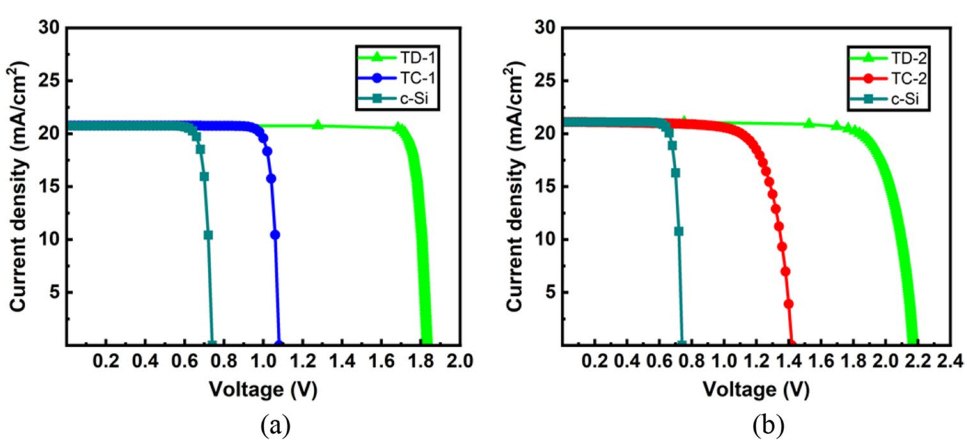

Fig. 11 J-V plots of **a** TD-1 and **b** TD-2, along with their respective TC and BC characteristics

Table 8 Comparison of TD's performance with reported experimental and simulated results

TD (TC/BC)	V_{OC}(V)	$J_{SC}(mA/cm^2)$	FF (%)	PCE (%)	Reference/ID	Year	Type of Analysis
Perovskite/Si	1.82	17.44	75.80	24.06	[50]	2023	Exp.
Perovskite/Si	1.75	16.36	80.33	23.00	[51]	2023	Exp.
Perovskite/Si	1.88	20.26	77.30	29.50	[2]	2022	Exp.
Perovskite/Si	1.80	18.81	77.50	26.30	[46]	2020	Exp.
Perovskite/Si	1.90	19.23	79.40	29.15	[47]	2020	Exp
GaInP/Si	2.07	17.04	88.00	31.10	[48]	2020	Exp.
Perovskite/Si	2.30	17.52	67.39	27.25	[52]	2023	Sim.
Perovskite/SnS	1.99	16.99	85.15	28.92	[38]	2022	Sim.
Perovskite/Si	1.87	20.3	84.70	32.20	[49]	2021	Sim.
Perovskite/Si	1.76	16.01	86.70	24.40	[30]	2021	Sim.
Lead-free double perovskite/c-Si	1.82	20.75	88.31	34.67	TD-2	*This work*	Sim.
Lead-free double perovskite/c-Si	2.16	21.10	79.68	36.88	TD-2	*This work*	Sim.

Exp. Experimental, *Sim.* Simulation

and $Cs_2AgBiBr_6/c-Si$ TDs exhibits a PCE of 34.67% (with $V_{OC}=1.82$ V, $J_{SC}=20.75$ mA/cm^2, FF = 88.31%) and 36.88% (with $V_{OC}=2.16$ V, $J_{SC}=21.105$ mA/cm^2, FF = 79.68%), respectively. J_{SC} values for both the devices are interestingly comparable. The V_{OC} and PCE values of $Cs_2AgBiBr_6/c-Si$ TD are higher as compared to $Cs_4CuSb_2Cl_{12}/c-Si$ TD, likely due to the greater thickness and bandgap values of $Cs_2AgBiBr_6$ compared with $Cs_4CuSb_2Cl_{12}$. Analysis of this study implies that enhancing the performance of double-perovskite TC is required to realize the overall benefits of the TD. The results reported here demonstrate that lead-free and stable double perovskite materials can act as an important absorber of sub-cell for highly efficient, commercially viable, non-toxic and eco-friendly tandem photovoltaic technologies. The insights derived from this device design study will aid researchers in designing and fabricating TDs with improved device performance for the real time photovoltaic applications.

Acknowledgements Authors are grateful to the Department of Science and Technology (DST), Govt. of India, for financial backing through DST SERB Project File No. SRG/2021/002110. Dr. Amitesh Kumar acknowledges DST SERB regarding the Start-up Research Grant, fostering research at NIT Patna. Mr. Pritam Kumar expresses gratitude for providing and supporting facilities for research extended by the Department of Electrical Engineering, NIT Patna. Prof. Marc Burgelman from the University of Gent, Belgium, is appreciated for providing the crucial open-source SCAPS-1D software essential to this work.

Author Contributions PK: Conceptualization, Methodology, Visualization, Investigation, Data curation, Software, Writing-original draft. AK: Conceptualization, Methodology, Formal analysis, Supervision, Reviewing and Editing.

Funding Authors are grateful to the Department of Science and Technology (DST), Govt. of India, for financial backing through DST SERB Project File No. SRG/2021/002110.

Data Availability No datasets were generated or analysed during the current study.

Declarations

Ethical Approval Not applicable.

Competing Interests The authors declare no competing interests.

References

1. Andreani LC, Bozzola A, Kowalczewski P et al (2019) Silicon solar cells: toward the efficiency limits. Adv Phys X 4:1548305. https://doi.org/10.1080/23746149.2018.1548305
2. Green MA, Dunlop ED, Siefer G et al (2023) Solar cell efficiency tables (Version 61). Prog Photovoltaics Res Appl 31:3–16. https://doi.org/10.1002/pip.3646
3. Alharbi FH, Kais S (2015) Theoretical limits of photovoltaics efficiency and possible improvements by intuitive approaches learned from photosynthesis and quantum coherence. Renew Sustain Energy Rev 43:1073–1089. https://doi.org/10.1016/j.rser.2014.11.101
4. Shockley W, Queisser HJ (1961) Detailed balance limit of efficiency of p-n junction solar cells. J Appl Phys 32:510–519. https://doi.org/10.1063/1.1736034
5. Zhang C, Gwamuri J, Andrews R, Pearce JM (2014) Design of multijunction photovoltaic cells optimized for varied atmospheric conditions. Int J Photoenergy 2014:1–8. https://doi.org/10.1155/2014/514962
6. Bremner SP, Levy MY, Honsberg CB (2008) Analysis of tandem solar cell efficiencies under AM1. 5G spectrum using a rapid flux calculation method. Prog Photovoltaics Res Appl 16:225–233. https://doi.org/10.1002/pip.799
7. Marti A, Araújo GL (1996) Limiting efficiencies for photovoltaic energy conversion in multigap systems. Sol Energy Mater Sol Cells 43:203–222. https://doi.org/10.1016/0927-0248(96)00015-3
8. Werner J, Niesen B, Ballif C (2018) Perovskite/silicon tandem solar cells: marriage of convenience or true love story?–An

overview. Adv Mater Interfaces 5:1700731. https://doi.org/10.1002/admi.201700731
9. Wang Z, Song Z, Yan Y et al (2019) Perovskite—a perfect top cell for tandem devices to break the S–Q limit. Adv Sci 6:1801704. https://doi.org/10.1002/advs.201801704
10. Leijtens T, Bush KA, Prasanna R, McGehee MD (2018) Opportunities and challenges for tandem solar cells using metal halide perovskite semiconductors. Nat Energy 3:828–838. https://doi.org/10.1038/s41560-018-0190-4
11. Lal NN, Dkhissi Y, Li W et al (2017) Perovskite tandem solar cells. Adv Energy Mater 7:1602761. https://doi.org/10.1002/aenm.201602761
12. Jost M, Kohnen E, Morales-Vilches AB et al (2018) Textured interfaces in monolithic perovskite/silicon tandem solar cells: Advanced light management for improved efficiency and energy yield. Energy Environ Sci 11:3511–3523. https://doi.org/10.1039/c8ee02469c
13. Islam T, Jani R, Islam AF et al (2021) Investigation of CsSn0.5Ge0.5I3-on-Si tandem solar device utilizing SCAPS simulation. IEEE Trans Electron Devices 68:618–625. https://doi.org/10.1109/TED.2020.3045383
14. Lakhdar N, Hima A (2020) Electron transport material effect on performance of perovskite solar cells based on CH3NH3GeI3. Opt Mater (Amst) 99:109517. https://doi.org/10.1016/j.optmat.2019.109517
15. Yu C (2019) Advances in modelling and simulation of halide perovskites for solar cell applications advances in modelling and simulation of halide perovskites for solar cell applications. J Phys Energy 1:022001. https://doi.org/10.1088/2515-7655/aaf143
16. Raj A, Kumar M, Bherwani H et al (2021) Evidence of improved power conversion efficiency in lead-free CsGeI 3 based perovskite solar cell heterostructure via scaps simulation. J Vac Sci Technol B 39:012401. https://doi.org/10.1116/6.0000718
17. Diouf B, Muley A, Pode R (2023) Issues, challenges, and future perspectives of perovskites for energy conversion applications. Energies 16:6498. https://doi.org/10.3390/en16186498
18. Mesquita I, Andrade L, Mendes A (2018) Perovskite solar cells: materials, configurations and stability. Renew Sustain Energy Rev 82:2471–2489. https://doi.org/10.1016/j.rser.2017.09.011
19. Chen Y, Zhang L, Zhang Y et al (2018) Large-area perovskite solar cells-a review of recent progress and issues. RSC Adv 8:10489–10508. https://doi.org/10.1039/c8ra00384j
20. Asmontas S, Mujahid M (2023) Recent progress in perovskite tandem solar cells. Nanomaterials 13:1886. https://doi.org/10.3390/nano13121886
21. Ji F, Boschloo G, Wang F, Gao F (2023) Challenges and progress in lead-free halide double perovskite solar cells. Sol RRL 7:2201112. https://doi.org/10.1002/solr.202201112
22. Mahajan P, Datt R, Chung Tsoi W et al (2021) Recent progress, fabrication challenges and stability issues of lead-free tin-based perovskite thin films in the field of photovoltaics. Coord Chem Rev 429:213633. https://doi.org/10.1016/j.ccr.2020.213633
23. Cai T, Shi W, Hwang S et al (2020) Lead-free Cs4CuSb2Cl12 layered double perovskite nanocrystals. J Am Chem Soc 142:11927–11936. https://doi.org/10.1021/jacs.0c04919
24. Mohandes A, Moradi M, Nadgaran H (2021) Numerical simulation of inorganic Cs2AgBiBr6 as a lead-free perovskite using device simulation SCAPS-1D. Opt Quantum Electron 53:1–22. https://doi.org/10.1007/s11082-021-02959-z
25. He Y, Xu L, Yang C et al (2021) Design and numerical investigation of a lead-free inorganic layered double perovskite cs4cusb2cl12 nanocrystal solar cell by scaps-1d. Nanomaterials 11:1–19. https://doi.org/10.3390/nano11092321
26. Yadav SC, Manjunath V, Srivastava A et al (2022) Stable lead-free Cs4CuSb2Cl12 layered double perovskite solar cells yielding theoretical efficiency close to 30%. Opt Mater (Amst) 132:112676. https://doi.org/10.1016/j.optmat.2022.112676
27. Pindolia G, Shinde SM, Jha PK (2022) Optimization of an inorganic lead free RbGeI3 based perovskite solar cell by SCAPS-1D simulation. Sol Energy 236:802–821. https://doi.org/10.1016/j.solener.2022.03.053
28. Gamal N, Sedky SH, Shaker A, Fedawy M (2021) Design of lead-free perovskite solar cell using Zn1-xMgxO as ETL: SCAPS device simulation. Optik (Stuttg) 242:167306. https://doi.org/10.1016/j.ijleo.2021.167306
29. Madani S, Tesfamichael T, Wang H, Motta N (2022) Study of Pb-based and Pb-free perovskite solar cells using Cu-doped Ni1-xO thin films as hole transport material. Ceram Int 48:15207–15217. https://doi.org/10.1016/j.ceramint.2022.02.051
30. Amri K, Belghouthi R, Aillerie M, Gharbi R (2021) Device optimization of a lead-free perovskite/silicon tandem solar cell with 24.4% power conversion efficiency. Energies 14:3383. https://doi.org/10.3390/en14123383
31. Kim K, Gwak J, Ahn SK et al (2017) Simulations of chalcopyrite/c-Si tandem cells using SCAPS-1D. Sol Energy 145:52–58. https://doi.org/10.1016/j.solener.2017.01.031
32. Mashot Jafar A, Khalaph KA, Moula Hmood A (2020) Lead-free perovskite and double perovskite solar cells. IOP Conf Ser Mater Sci Eng 765:1–11. https://doi.org/10.1088/1757-899X/765/1/012047
33. Loper P, Stuckelberger M, Niesen B et al (2015) Complex refractive index spectra of CH3NH3PbI3 perovskite thin films determined by spectroscopic ellipsometry and spectrophotometry. J Phys Chem Lett 6:66–71. https://doi.org/10.1021/jz502471h
34. Al-Mousoi AK, Mohammed MKA, Kumar A et al (2023) Understanding auger recombination in perovskite solar cells. Phys Chem Chem Phys 25:16459–16468. https://doi.org/10.1039/d3cp00441d
35. Madan J, Shivani, Pandey R, Sharma R (2020) Device simulation of 17.3% efficient lead-free all-perovskite tandem solar cell. Sol Energy 197:212–221. https://doi.org/10.1016/j.solener.2020.01.006
36. Sinha NK, Ghosh DS, Khare A (2022) Role of built-in potential over ETL/perovskite interface on the performance of HTL-free perovskite solar cells. Opt Mater (Amst) 129:112517. https://doi.org/10.1016/j.optmat.2022.112517
37. Yoshikawa K, Kawasaki H, Yoshida W et al (2017) Silicon heterojunction solar cell with interdigitated back contacts for a photoconversion efficiency over 26%. Nat Energy 2:17032. https://doi.org/10.1038/nenergy.2017.32
38. Jafarzadeh F, Aghili H, Nikbakht H, Javadpour S (2022) Design and optimization of highly efficient perovskite/homojunction SnS tandem solar cells using SCAPS-1D. Sol Energy 236:195–205. https://doi.org/10.1016/j.solener.2022.01.046
39. Abdelaziz S, Zekry A, Shaker A, Abouelatta M (2022) Investigation of lead-free MASnI3-MASnIBr2 tandem solar cell: numerical simulation. Opt Mater (Amst) 123:111893. https://doi.org/10.1016/j.optmat.2021.111893
40. Eperon GE, Stranks SD, Menelaou C et al (2014) Formamidinium lead trihalide: a broadly tunable perovskite for efficient planar heterojunction solar cells. Energy Environ Sci 7:982–988. https://doi.org/10.1039/c3ee43822h
41. Dastan D, Mohammed MKA, Al-Mousoi AK et al (2023) Insights into the photovoltaic properties of indium sulfide as an electron transport material in perovskite solar cells. Sci Rep 13:1–11. https://doi.org/10.1038/s41598-023-36427-3
42. Salem MS, Shaker A, Zekry A et al (2021) Analysis of hybrid hetero-homo junction lead-free perovskite solar cells by scaps simulator. Energies 14:1–23. https://doi.org/10.3390/en14185741
43. Abdelaziz S, Zekry A, Shaker A, Abouelatta M (2020) Investigating the performance of formamidinium tin-based perovskite solar

cell by SCAPS device simulation. Opt Mater (Amst) 101:109738. https://doi.org/10.1016/j.optmat.2020.109738
44. Sengar BS, Garg V, Kumar A, Dwivedi P (2021) Numerical simulation: design of high-efficiency planar p-n homojunction perovskite solar cells. IEEE Trans Electron Devices 68:2360–2364. https://doi.org/10.1109/TED.2021.3066454
45. Li ZQ, Ni M, Feng XD (2019) Simulation of the Sb2Se3 solar cell with a hole transport layer. Mater Res Express 7:1–9. https://doi.org/10.1088/2053-1591/ab5fa7
46. Lamanna E, Matteocci F, Calabrò E et al (2020) Mechanically stacked, two-terminal graphene-based perovskite/silicon tandem solar cell with efficiency over 26%. Joule 4:865–881. https://doi.org/10.1016/j.joule.2020.01.015
47. Al-Ashouri A, Köhnen E, Li B et al (2020) Monolithic perovskite/silicon tandem solar cell with > 29% efficiency by enhanced hole extraction. Science 370:1300–1309. https://doi.org/10.1126/science.abd4016
48. Benaicha M, Dehimi L, Pezzimenti F, Bouzid F (2020) Simulation analysis of a high efficiency GaInP/Si multijunction solar cell. J Semicond 41:1–6. https://doi.org/10.1088/1674-4926/41/3/032701
49. Sarker S, Islam MT, Rauf A et al (2021) A SCAPS simulation investigation of non-toxic MAGeI3-on-Si tandem solar device utilizing monolithically integrated (2-T) and mechanically stacked (4-T) configurations. Sol Energy 225:471–485. https://doi.org/10.1016/j.solener.2021.07.057
50. Dai L, Li S, Hu Y et al (2023) Three-terminal monolithic Perovskite/silicon tandem solar cell exceeding 29% power conversion efficiency. ACS Energy Lett 8:3839–3842. https://doi.org/10.1021/acsenergylett.3c01347
51. Jung ED, Kim CU, Noh YW et al (2023) Aesthetic and efficient perovskite/Si tandem solar cells using luminescent down-shifting textured anti-reflection films. EcoMat 5:1–11. https://doi.org/10.1002/eom2.12399
52. Wang Y, Tian H, Zhang D et al (2023) Study on high – efficiency double perovskite / silicon heterojunction tandem cells with sb – doped Cs2AgBiBr6. J Electron Mater 52:7728–7739. https://doi.org/10.1007/s11664-023-10692-4